Primary Frequency Control Scheme for a Fixed-Speed Dish-Stirling Solar-Thermal Power Plant

Yang Li, *Member, IEEE,* San Shing Choi, *Senior Member, IEEE,*
and D. Mahinda Vilathgamuwa *Senior Member, IEEE*

Abstract—The ability of induction generator-based dish-Stirling (DS) solar-thermal power plant in providing primary frequency control is examined. A dynamic model of the power plant is developed in which the receiver/absorber temperature of the Stirling engine is allowed to vary. Primary frequency control is achieved through the adaptive regulation of the receiver temperature set-point and the droop setting of the output power-temperature characteristics of the DS system. However, the penetration level of the solar-thermal generation into grid system has to be constrained to avoid the onset of instability due to the nonminimum phase characteristics of the DS system. Transient droop compensation technique is then proposed to alleviate the instability issue, and results in an increase in the allowable DS penetration level.

Index Terms—Dish-Stirling system, fixed-speed induction generator, frequency control, solar-thermal power generation.

I. INTRODUCTION

IN recent years, one witnesses the ever-increasing proportion of the renewable generation in many electricity supply networks. Amongst the various concentrated solar power (CSP) technologies, the dish-Stirling (DS) solar-thermal generating system has a unique construction: a parabolic dish-like reflector concentrates sunlight onto a small area called the receiver located at the focal point of the reflector. The receiver serves as the heat source for a Stirling engine which drives an electric generator. This system is capable of operating at high efficiency and releases nearly no emission [1]. The amount of CSP generation in grid systems is expected to increase: for instance, the recently-announced construction of 12 large-scale CSP plants in Australia is a case in point. However, the solar irradiance input to the CSP system, such as that of the DS generators, tends to be unsteady and is uncertain. Consequently it would induce undesirable frequency perturbations in the interconnected network. As the penetration level of the CSP generation increases, a stage will be reached when the CSP generators will be forced to contribute in the provision of network system frequency support [2]–[4]. Notwithstanding the works described in [2]–[5] wherein the assumed DS plant model from [6] is used, the frequency regulating ability of the DS power plants has yet to be rigorously analyzed primarily due to the lack of suitable DS plant model. The purpose of the present investigation is to fill this gap.

The authors are with the School of Electrical Engineering and Computer Science, Queensland University of Technology, Brisbane, QLD 4001, Australia (e-mail: yangli@ieee.org; sanshing.choi@qut.edu.au; mahinda.vilathgamuwa@qut.edu.au).

As frequency control is closely associated with the mechanism to achieve load-generation real power balance, the key task is to find effective ways to regulate the generated power of the DS system in response to the frequency variations. A conventional DS system is equipped with the technologically well-proven and economical squirrel-cage induction generators (SCIGs). However, SCIGs operate over a relatively narrow speed range and therefore, such a fixed-speed dish-Stirling system (FSDS) is incapable of providing significant level of frequency regulation through the adjustments of the generator speed. Possible ways to mitigate such a deficiency include the replacement of the SCIGs with variable-speed generators [6], [7] and/or the use of energy storage systems to provide the necessary spinning reserve. However, these remedies would incur increased costs and the reliability of the overall system could be reduced. The more attractive option is to fully exploit the potential of the FSDS on frequency regulation, and to minimize the need to replace and/or to add major equipment.

As shall be seen later, the output power of the FSDS can be varied by controlling several state variables within its thermodynamic system, without the need to install additional hardware. To evaluate the potential of such strategy, a suitable mathematical model of the FSDS is required. As explained in the authors previous work [8], approximate average-value model of the Stirling engine is advantageous over the complex multi-cylinder thermodynamic model because the approximate model can lead to a simpler approach to analysis and controller design. Indeed, several average-value models have been derived to meet the respective research purposes [7]–[9]. However, the behavior of the FSDS under variable receiver temperature operating mode has not been investigated in [7]–[9] where the temperature is invariably assumed to be very close to its maximum allowable value so as to achieve high thermal efficiency. Although varying temperature has been considered as one of the effective methods to regulate the engine power [10], to do so to achieve the frequency control objectives has not been fully studied in the open literature.

In comparison to the cited works, major contributions of the present investigation are: 1) a nonlinear FSDS model is developed from the thermodynamic principles governing the FSDS. The model is suitable for use in network primary frequency control studies in which the receiver temperature is allowed to vary; 2) The FSDS is shown to exhibit non-minimum phase characteristics when the generator operates to meet grid-code frequency control requirement. Whence

the maximum solar insolation and allowable FSDS penetration levels to ensure stable FSDS operation are determined from small-signal analysis; 3) An enhanced droop primary frequency control scheme is proposed to increase the stability margin of the FSDS. The control scheme permits higher FSDS generation participation in grid systems.

The remainder of this paper is organized as follows. In Section II, a brief explanation of the FSDS is presented and the FSDS model is developed to include the effects of lower receiver temperature on the output power of the FSDS. Section III presents the steady-state analysis of the FSDS operation, using the developed model. Section IV develops an adaptive droop control scheme to provide primary frequency support from the FSDS so as to comply with the frequency response requirement demanded by grid codes. Section V studies the performance of a proposed scheme in which the droop control is augmented by transient droop compensation for grid-connected FSDS system. Examples of dynamic simulation study are included in Section VI to verify the validity of the developed model and the proposed design methodology. Section VII summarizes the main findings.

II. MODELING OF THE FSDS

A. FSDS Operating Under Maximum Allowable Temperature

The modeling and control of such a DS system has been addressed in [8], [11], [12] under the assumption that the generating system operates near the maximum allowable temperature $T_{h,\max}$. The energy conversion process of such a DS system consists of three parts. First, the parabolic dish alluded to earlier collects, reflects and concentrates the solar irradiance I onto a heat receiver attached to the absorber tubes of the Stirling engine. This heat transfer process is described by [8]

$$(T_{\text{rec}}/K_{\text{rec}})\dot{T}_h = K_{\text{con}}I - Q_h - Q_L \tag{1}$$

$$Q_L = (T_h - T_a)/K_{\text{rec}} \tag{2}$$

where Q_h is the thermal power absorbed by the engine, Q_L is heat losses, and T_h and T_a are the receiver and the ambient temperature respectively. Constants T_{rec}, K_{rec} and K_{con} embody the heat transfer characteristics of the receiver.

Next, a Stirling engine converts the heat into mechanical energy. In authors previous work [9], an average-value model of the most commonly-used double-acting kinematic Stirling engine was derived. The relevant expressions are:

$$Q_h = \eta_h[K_h p_{\text{mean}}\omega_m + A(gA) + Cp_{\text{mean}}\dot{T}_h] \tag{3}$$

$$P_m = \eta_m K_m p_{\text{mean}}\omega_m \tag{4}$$

$$(gA) = \dot{M} = (1/K_p)\dot{p}_{\text{mean}} \tag{5}$$

$$T_v(g\dot{A}) = -(gA) + K_v c \tag{6}$$

where the thermal power Q_h and the mechanical power P_m are functions of the thermodynamic state variables including the engine speed ω_m, mean pressure p_{mean} of the working gas in the engine cylinders, temperature T_h, and their derivatives. η_h and η_m are two efficiency coefficients introduced to account

for the steady-state thermal and mechanical losses, which are expressed as

$$\eta_h = \sum_{i=0}^{1}\sum_{j=0}^{1} a_{ij}p_{\text{mean}}^i\omega_m^j/(K_h p_{\text{mean}}\omega_m) \tag{7}$$

$$\eta_m = \sum_{i=0}^{1}\sum_{j=0}^{2} b_{ij}p_{\text{mean}}^i\omega_m^j/(K_m p_{\text{mean}}\omega_m) \tag{8}$$

where a_{ij} and b_{ij} are two groups of multivariable polynomial coefficients obtained from engine performance map. Constants K_h, K_m, A and C are defined in [7], where the steady-state behavior of the developed model has been verified to be accurate by a DS emulator. In (5), K_p represents a proportional relationship between the total mass M of the working gas and p_{mean}. Thus, p_{mean} can be regulated by manipulating the net gas flow rate gA using a solenoid valve system with external gas tanks, and K_v, T_v, and c are the relevant gain, time constant, and control command of this valve system.

Finally, a Stirling engine-driven SCIG converts the mechanical energy into electricity. As shown in [7]–[9], the developed model is more suitable than the detailed adiabatic model used in [11], [12], in the course of developing control systems for the DS generators.

B. FSDS Operating Under Variable Temperature

The aim of this study is to investigate how the output power Pm of the FSDS can be manipulated to support grid frequency, by allowing the variation of receiver temperature T_h of the FSDS. When T_h falls below $T_{h,\max}$, the model given in Section II-A is invalid and it needs to be modified. First, the nonlinear characteristics of radiation heat loss at temperature lower than $T_{h,\max}$ means that the normalized equation (36) derived in Appendix A is to replace (2) and it yields

$$Q_L(T_h) = K_{\text{rec1}}(T_h - T_a) - K_{\text{rec2}}(T_h^4 - T_a^4). \tag{9}$$

The first and the second terms on the RHS of (9) embody the effects of heat losses due to convection/conduction and radiation respectively.

Second, the temperature affects the thermal efficiency of the Stirling engine. A commonly used expression to estimate the output mechanical power P_m of the Stirling engine is given in [13], where P_m is proportional to $(T_h - T_k)/(T_h + T_k)$. The cooler space temperature T_k of the Stirling engine is considered constant. Hence, the efficiency η_m in (8) shall be modified to

$$\eta_m = \frac{1}{K_m}\sum_{i=0}^{1}\sum_{j=0}^{2} b_{ij}p_{\text{mean}}^{i-1}\omega_m^{j-1}\left(\frac{T_h - T_k}{T_h + T_k}\frac{1 + T_k}{1 - T_k}\right) \tag{10}$$

where a constant gain $(1 + T_k)/(1 - T_k)$ is used to ensure that at $T_h = T_{h,\max} = 1$ p.u., (10) is identical to (8).

In summary, the complete FSDS model for the primary frequency support study consists of (1), (3)–(7), (9) and (10), based which steady-state analysis will be carried out next.

III. STEADY-STATE ANALYSIS OF THE FSDS

A. Output Power-Receiver Temperature Relationship

The focus of this subsection is to derive the steady-state functional relationship between the output power of the Stirling engine and the receiver temperature of the FSDS. Consider $\omega_m = 1$ p.u. for the fixed-speed operation and setting all the d/dt terms in (1), (3)–(5), and (6) to zero, the following steady-state relationship can be derived:

$$P_m = \sum_{j=0}^{2} (b_{0j} + b_{1j}p_{\text{mean}}) \frac{T_h - T_k}{T_h + T_k} \frac{1 + T_k}{1 - T_k} \quad (11)$$

$$Q_h = a_{00} + a_{01} + (a_{10} + a_{11})p_{\text{mean}} = K_{\text{con}}I - Q_L(T_h). \quad (12)$$

Note that (11) and (12) contain nonlinear terms with respect to T_h. To simplify the analysis, a second-degree polynomial is used to approximate the nonlinear term in (11), i.e.,

$$\frac{T_h - T_k}{T_h + T_k} \frac{1 + T_k}{1 - T_k} = k_{m0} + k_{m1}T_h + k_{m2}T_h^2. \quad (13)$$

Substituting (13) into (11), P_m can expressed as

$$P_m = d_{00} + d_{01}T_h + d_{02}T_h^2 + (d_{10} + d_{11}T_h + d_{12}T_h^2)p_{\text{mean}} \quad (14)$$

where the polynomial coefficients d_{ij} are defined as

$$d_{ij} = k_{mj}(b_{i0} + b_{i1} + b_{i2}) \ (i = 0, 1 \text{ and } j = 0, 1, 2)$$

At maximum insolation, $I = 1$ p.u. Substituting $T_h = p_{\text{mean}} = P_m = 1$ p.u. into (13) and (14), it can be readily shown that $k_{m0} + k_{m1} + k_{m2} = 1$ and $d_{00} + d_{10} + d_{01} + d_{11} + d_{02} + d_{12} = 1$.

Next, using (9) and (12), one can obtain the expression for p_{mean} as a function of I and T_h, whence,

$$p_{\text{mean}} = \frac{K_{\text{con}}I - Q_L(T_h) - a_{00} - a_{01}}{a_{10} + a_{11}}. \quad (15)$$

Substituting (15) into (14) to eliminate p_{mean}, thus the output mechanical power P_m of the Stirling engine is

$$\begin{aligned} P_m(I, T_h) &= (d_{10} + d_{11}T_h + d_{12}T_h^2)/(a_{10} + a_{11}) \\ &\times [K_{\text{con}}I - Q_L(T_h) - (a_{00} + a_{01})] \\ &+ d_{00} + d_{01}T_h + d_{02}T_h^2. \end{aligned} \quad (16)$$

As can be seen in (16), the insolation level I and temperature T_h are the two variables governing P_m. As I is considered an uncontrollable input in this study, the potential of controlling P_m through the manipulation of T_h shall be examined next.

B. Feasible Operating Zone of FSDS

With the derived steady-state relationship (16), one can obtain a family of P_m–T_h curves at various insolation levels I. Example of such a family of P_m–T_h curves, with each curve corresponding to a given I, is shown by the dashed lines in Fig. 1. The values of the FSDS parameters used to construct the figure are given in Appendix B. In practice, however, the working gas mean pressure p_{mean} has to be limited between the pressure in the low pressure tank p_{min} and the pressure in the high pressure tank p_{max}. Concurrently,
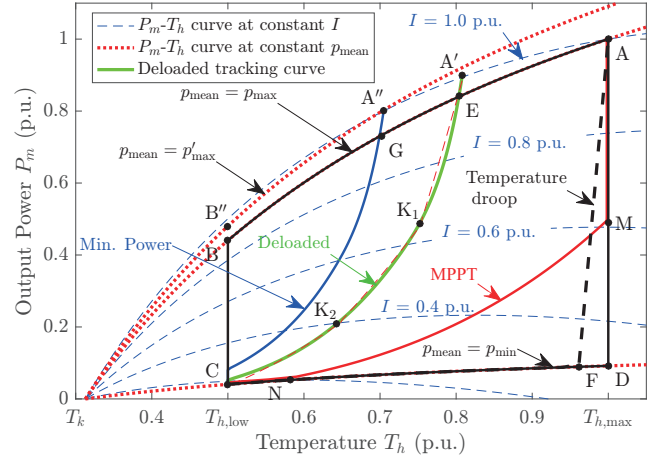

Fig. 1. Feasible operating zone: FSDS operating under variable temperature.

the receiver temperature, T_h, is constrained to lie between the low temperature limit $T_{h,\text{low}}$ which enables the Stirling engine to generate power, and the maximum temperature $T_{h,\text{max}}$ the receiver can tolerate. $T_{h,\text{low}}$ must be higher than the cooler space temperature T_k of the Stirling engine so as to comply with the second law of thermodynamics. $T_{h,\text{max}}$ is governed by the thermal characteristics of the material used to construct the receiver wall and absorber. Hence the area ABCD in Fig. 1 defines the steady-state feasible operating zone (FOZ) of the FSDS, in consideration of these constraints. The various segments of the boundary of the FOZ are:

- A–B, applies due to the maximum mean pressure p_{max};
- B–C, dictates by the lower temperature limit $T_{h,\text{low}}$;
- C–D, pertains to the minimum mean pressure p_{min};
- D–A, governs by the maximum temperature $T_{h,\text{max}}$.

The boundaries AB and CD can be obtained by letting $p_{\text{mean}} = p_{\text{max}}$ and $p_{\text{mean}} = p_{\text{min}}$ respectively in (14), evaluated over a range of T_h.

From Fig. 1, it can be seen that under a given insolation level, it is possible to regulate P_m by varying the working temperature T_h. Furthermore, on each P_m–T_h curve at constant I, there exists an optimal temperature for which the maximum power is obtained. This maximum power point tracking (MPPT) locus, as depicted in Fig. 1, can be obtained by letting $\partial P_m/\partial T_h = 0$ in (16) with given value of I. This characteristics is common for all CSP technologies and can be used to determine the appropriate working temperature of a CSP system [14]. Suppose the MPPT locus intersects the FOZ boundaries DA and CD at points M and N respectively. In view of the constraints placed on the p_{mean} and T_h, the actual MPPT trajectory would then follow the curve AMNC in Fig. 1. AM is obtained using (16) for a range of I when $T_h = T_{h,\text{max}}$ and NC is formed using (14) for a range of T_h when $p_{\text{mean}} = p_{\text{min}}$, respectively. Note the FOZ and MPPT locus differ from those obtained in [8] where the FOZ and the MPPT locus were derived under the constant-temperature and variable-speed DS operations.
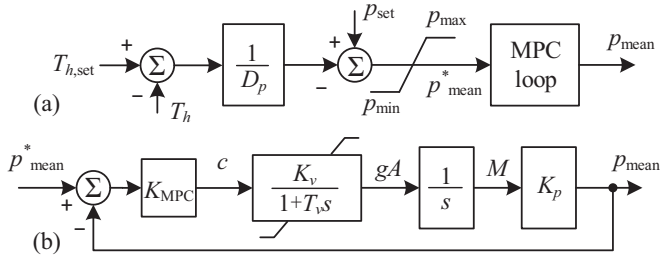
Fig. 2. (a) Temperature and (b) mean pressure controllers featuring the droop characteristics and pressure/valve limits. $K_{\text{MPC}} = 1/(2T_v K_v K_p)$.

Fig. 3. A simplified frequency response requirement stipulated in grid codes.

C. A Conventional Approach to Temperature Control

Based on the above analysis, it is clear P_m can be regulated through the manipulation of the receiver temperature. As an alternative to MPPT operation, a simpler temperature control scheme is to follow the locus AFC in Fig. 1. AF embodies a droop characteristic which allows a slight drop of temperature setting from $T_{h,\max}$ when the insolation I is less than 1 p.u. [8]. Fig. 2 shows the block diagram of implementing this temperature control objective through the regulating actions of the working gas mean pressure controller (MPC) which has the constant gain $K_{\text{MPC}} = 1/(2T_v K_v K_p)$. Accordingly, the solenoid valve system control command signal c alluded to earlier is

$$c = K_{\text{MPC}}(p^*_{\text{mean}} - p_{\text{mean}}). \qquad (17)$$

The dynamics of the inner MPC loop is much faster than that of the temperature–frequency control, thus p_{mean} can be considered identical to its set point p^*_{mean}. Whence the steady-state droop characteristics of the temperature controller shown in Fig. 2 can be expressed as

$$p_{\text{mean}} = p^*_{\text{mean}} = p_{\text{set}} - (T_{h,\text{set}} - T_h)/D_p \qquad (18)$$

where $T_{h,\text{set}}$ and p_{set} correspond to the steady-state T_h and p_{mean} at $I = 1$ p.u. respectively. The temperature–pressure droop setting is defined as $D_p = (T_{h,\max} - T_{h,\min})/(p_{\max} - p_{\min})$, where $T_{h,\min}$ is the temperature at $p_{\text{mean}} = p_{\min}$. Substituting (18) into (14), P_m can be expressed as a function of T_h, i.e.,

$$P_m = \left(\frac{D_p p_{\text{set}} - T_{h,\text{set}}}{D_p} + \frac{T_h}{D_p} \right)(d_{10} + d_{11}T_h + d_{12}T_h^2) + d_{00} + d_{01}T_h + d_{02}T_h^2. \qquad (19)$$

Setting $T_{h,\text{set}} = p_{\text{set}} = 1$ p.u. according to the conventional design approach as in [7] and using (19), the slope of AF is approximated by evaluating the value of dP_m/dT_h at $T_h \approx 1$ p.u.

$$\left. \frac{dP_m}{dT_h} \right|_{T_h=1} = \frac{d_{10} + d_{11} + d_{12}}{D_{p,\text{AF}}} + (d_{11} + 2d_{12}) \approx \frac{1}{D_{p,\text{AF}}}. \qquad (20)$$

In (20), $D_{p,\text{AF}}$ is droop D_p of AF, and it can be determined to enhance the dynamic response characteristics of the DS system under the temperature control mode [8]. In obtaining (20), one uses the fact that d_{00}, d_{01}, d_{02} and $D_{p,\text{AF}}$ are much smaller than 1 and $d_{10} + d_{11} + d_{12} \approx 1$. The equation shows the slope of AF approximately equals the reciprocal of $D_{p,\text{AF}}$.
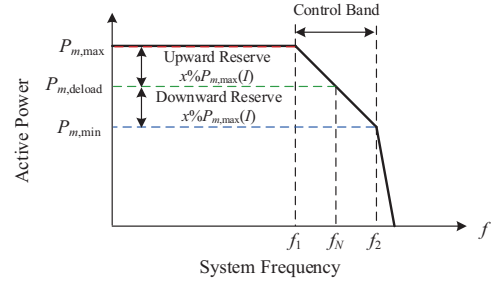
When the insolation level is below that corresponding to point F, the minimum mean pressure limit $p_{\min}$ is reached and in order to maintain the power balance, T_h shall fall rapidly and the operating point shall move along the minimum mean pressure line FC. In practice, low insolation level occurrences often arise e.g., during the starting-up of the DS system in the early morning and its shutdown in the evening, or during cloudy days. As a consequence, the inclusion of the FC provides a smooth transition in the operating temperature as the isolation level varies at the low levels.

IV. FSDS Primary Frequency Control Scheme

Primary frequency control is often mandated in grid codes for generating units, in the form of the unit output power C system frequency droop curve and unit response time [15], [16]. In this section, a frequency control scheme is proposed which will involve the minimal modification of the conventional FSDS temperature control scheme shown in Section III-C.

A. Feasible Deloaded Operating Zone

In this study, the purpose of the receiver temperature control is to regulate P_m so that the FSDS can contribute to frequency support. Fig. 3 the frequency regulating ability required on generators, as stipulated in grid codes on frequency regulation such as in [16]. Within the control band f_1 and f_2, a droop characteristics prescribes the requirement in the provision of the upward and downward reserve powers for frequency support ancillary service. The corresponding power settings at f_1 and f_2 are denoted by $P_{m,\max}$ and $P_{m,\min}$ respectively, while $f_N = 1$ p.u. is the nominal system frequency. In the event $f > f_2$ or $f < f_1$, the system is considered under extreme contingency. This situation is not dealt with in the present study.

In view of the FOZ in Fig. 1, the maximum power $P_{m,\max}$ can be set to track the constrained MPPT locus AMNC at given I. So $P_{m,\max}$ would increase with I and hence, $P_{m,\max}$ is more appropriately labelled as $P_{m,\max}(I)$. To cater for the upward reserve as required in Fig. 3, this can be accommodated by deloading the FSDS. In Fig. 1, the deloaded operation is governed by the curve EC wherein the deloaded power $P_{m,\text{deload}}(I)$ is

$$P_{m,\text{deload}}(I) = (1 - x\%)P_{m,\max}(I). \qquad (21)$$

In developing the deloaded curve, $x\% P_{m,\max}(I)$ is the maximum amount of upward reserve power prescribed under
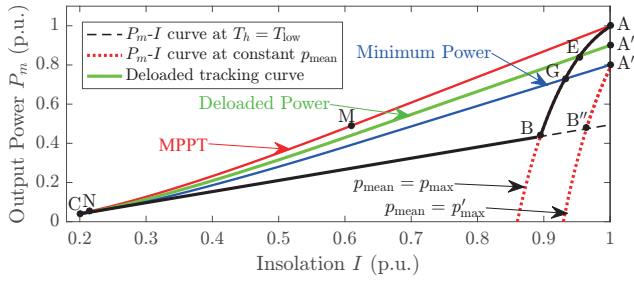
Fig. 4. Power vs. insolation relationship of FSDS system.

Fig. 5. Families of P_m–T_h curves obtained by varying (a) $T_{h,\text{set}}$; (b) D_p.

Fig. 6. Proposed primary frequency control loop of FSDS.

the grid code. The corresponding T_h at the deloaded operating points can be obtained using (16) by setting $P_m(I, T_h) = P_{m,\text{deload}}$ at the given I. Operating point E on the deloaded power curve corresponds to the maximum pressure condition.

Similarly, the minimum power $P_{m,\text{min}}(I)$ used for downward regulation is

$$P_{m,\text{min}}(I) = (1 - 2x\%)P_{m,\text{max}}(I). \tag{22}$$

Whence the power–frequency droop setting R_{DS} of the control band in Fig. 3 is

$$R_{\text{DS}} = \frac{f_N - f_1}{(P_{m,\text{max}} - P_{m,\text{deload}})/P_{m,\text{max}}} = \frac{1 - f_1}{x\%}. \tag{23}$$

Expressed in a different way, the P_m vs. I relationship for the various curves shown in Fig. 1 is presented in Fig. 4. It shows the possible range of power variations at different insolation levels. The area AMNCBA is that part of FOZ above the MPPT locus shown in Fig. 1. In Fig. 4, EC and GC represent the $P_{m,\text{deload}}(I)$ and $P_{m,\text{min}}(I)$ curves respectively. The operating zone AMCA″A, which is intended for primary frequency control, has the point A″ being the value of $P_{m,\text{min}}(I)$ at the maximum insolation level $I = 1$ p.u. However, the area AGA″A falls outside of the FOZ, due to the limit $p_{\text{max}} = 1$ p.u. (line AB). Hence, the required downward and upward regulation cannot be met when the insolation level exceeds that corresponding to point G and E, respectively. So the high-pressure tank pressure limit p_{max} is treated as a parameter to be determined during the design stage of the FSDS. Accordingly and as shown in Fig. 4, p_{max} is increased to a higher value p'_{max}. p'_{max} is evaluated for the operating point A″ using (15) and (16) with $I = 1$ p.u. and $P_m = (1 - 2x\%)P_{m,\text{max}}(I)$. So the whole deloaded operating zone AMCA″A is now feasible and the FSDS can meet the spinning reserve requirement stipulated as in Fig. 3.

B. Setting the Deloaded P_m–T_h Curve

The previous section shows that the feasible deloaded operating zones is AMCA″A, within which lies the deloaded P_m–T_h curve A′C. To ensure the operating state of the FSDS will track the curve A′C as I varies, T_h has to be adjusted accordingly. The commonly used static tracking methods, such as look-up table, cannot be adopted here without altering the control structure of Fig. 2. Instead, the preferred method is to adaptively tune the temperature controller in Fig. 2. From (19) and for a fixed p_{set} of 1 p.u., it is observed only the parameters
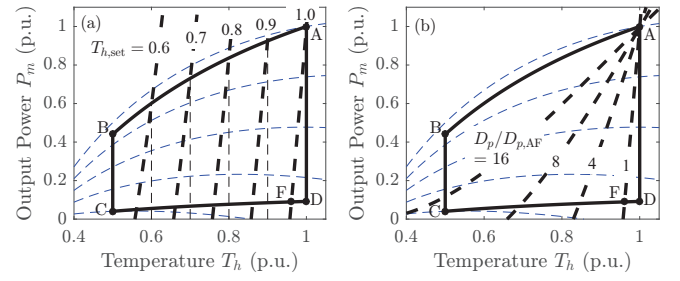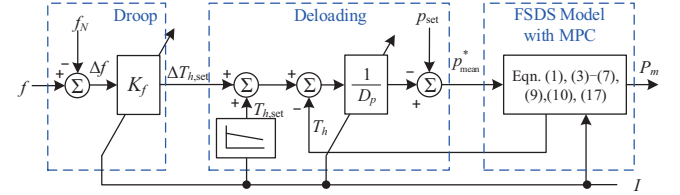
$T_{h,\text{set}}$ and D_p can affect the shape of the P_m–T_h curve. Indeed, by varying $T_{h,\text{set}}$ but maintaining $D_p = D_{p,\text{AF}}$, a family of P_m–T_h curves can be obtained. This is shown in Fig. 5 (a) when $T_{h,\text{set}}$ varies in 0.1 p.u. steps. The curves are parallel and to the left of AF and have the same slope $D_{p,\text{AF}}$ as for AF. On the other hand, by maintaining $T_{h,\text{set}} = 1$ p.u. and increasing D_p, another family of P_m–T_h curves as depicted in Fig. 5 (b) can be obtained. The new curves can be obtained by rotating AF about point A to reduce the slope to the specific $1/D_p$. In (18), when $p_{\text{mean}} = p_{\text{set}} = 1$ p.u., $T_h = T_{h,\text{set}}$. Thus, $T_{h,\text{set}}$ is the temperature at the point of intersection of P_m–T_h curve and the curve AB. The corresponding P_m at the intersection, denoted as $P_{m,\text{set}}$, can be obtained by substituting $p_{\text{mean}} = 1$ and $T_h = T_{h,\text{set}}$ into (14).

In view of the above, a set of D_p and $T_{h,\text{set}}$ governs the deloaded curve A′C at the nominal frequency. A′C will assume the set-point values $(T_{h,\text{set}}, P_{m,\text{set}})$ when $p_{\text{mean}} = 1$ p.u. In this study, A′C is approximated by n-segments (A′K_1, K_1K_2, …, K_{n-1}C), and each segment is determined by a specific set of $(D_p, T_{h,\text{set}})$. The values of D_p and $T_{h,\text{set}}$ of each segment can be readily calculated by substituting the values of P_m and T_h corresponding to the two end points of the segment into (19), and then solving the resulting simultaneous equations.

C. An Adaptive Droop Control Scheme

Comparing Fig. 5 (a) and (b), it can be seen that regulating $T_{h,\text{set}}$ is more effective in realizing the deloaded curve A′C than by regulating through D_p: it is difficult to regulate P_m at high I levels through varying D_p, as can be seen from Fig. 5 (b) the family of curves are clustered at high I. Hence, an adaptive supplementary control loop to effect the primary frequency control is proposed as shown in Fig. 6 wherein both $T_{h,\text{set}}$ and D_p are varied in accordance to I. In regulating $T_{h,\text{set}}$, the parameter K_f shown in Fig. 6 governs the extent of P_m variation in response to frequency perturbation Δf, viz.

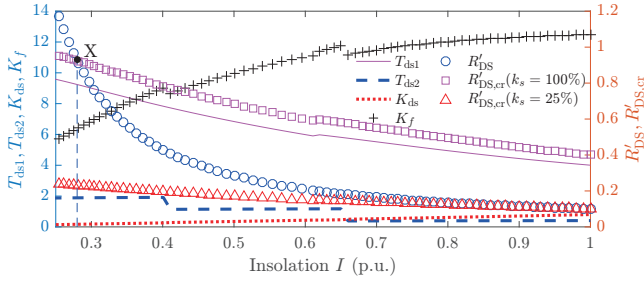$$\Delta T_h \approx \Delta T_{h,\text{set}} = K_f \Delta f. \tag{24}$$

Fig. 7. Relationships between droops, T_{ds1}, T_{ds2}, K_{ds2}, and K_f with I: line A′C is approximated by 3 segments: $I \leq 0.4$, $0.4 < I \leq 0.65$, $0.65 < I \leq 1$.

From the definition of droop in (23), thus,

$$K_f = \frac{\Delta T_h}{\Delta f} = \frac{\Delta T_h}{\Delta P_m}\frac{x\%}{1-f_1}P_{m,\max} \approx \frac{1}{k}\frac{x\%}{1-f_1}P_{m,\max} \quad (25)$$

where $k = dP_m/dT_h$ is the slope of the deloaded curve A′C at the given I. So k can be readily obtained. As k and $P_{m,\max}$ are both functions of I, K_f is a function of I too, as shown in Fig. 7. K_f has to be tuned in accordance of I. One possible way to overcome this rather cumbersome practice is to assume a constant value for K_f over a given range of I.

V. SMALL-SIGNAL STABILITY ANALYSIS OF FSDS PRIMARY FREQUENCY CONTROL IN GRID SYSTEM

A. FSDS Primary Frequency Control in Isolated System

An adaptive primary frequency control scheme has been developed for the FSDS, as shown in Fig. 6. In this section, it will be shown that valuable insights can be gained by carrying out small-signal analysis of the adaptive droop control scheme. Firstly, the transfer function $\Delta P_m(s)/\Delta f(s)$ can be obtained by linearizing the system model (1), (3)–(7), (9), (10), (17), (18), and (24) at specific insolation level I, i.e.,

$$\frac{\Delta P_m(s)}{\Delta f(s)} = \frac{\Delta T_{h,\mathrm{set}}(s)}{\Delta f(s)}\frac{\Delta P_m(s)}{\Delta T_{h,\mathrm{set}}(s)} = K_f \cdot K_{ds}\frac{1 - T_{ds1}s}{1 + T_{ds2}s}. \quad (26)$$

The detailed derivation of transfer function $\Delta P_m(s)/\Delta T_{h,\mathrm{set}}(s)$ is given in the Appendix C. The steady-state gain of (26) can be expressed in terms of the power–frequency droop R_{DS} which is given in (23)

$$K_f K_{ds} = \frac{\Delta P_m(s=0)}{\Delta f(s=0)} = \frac{P_{m,\max}(I)}{R_{DS}} = \frac{1}{R'_{DS}}. \quad (27)$$

As defined in (27), $R'_{DS} = R_{DS}/P_{m,\max}(I)$. R'_{DS} is the power-frequency droop setting defined in terms of the FSDS maximum power $P_{m,\max}(I)$ at given I. Unlike a conventional synchronous generator in which the unit droop setting is a constant, since $P_{m,\max}(I)$ increases with I, the effective droop R'_{DS} of the FSDS decreases as I increases. Also as shown in Appendix C and Fig. 7, the parameters T_{ds1}, T_{ds2}, and K_{ds} in the transfer function (26) are nonlinear functions of I.

Next, consider the dynamic characteristics of the FSDS. The appearance of an RHP zero at $s = T_{ds1}$ in (26) signifies the FSDS is a nonminimum phase (NMP) system, a characteristic which could prolong the response of the FSDS to disturbances and may even induce instability on the operation of the FSDS. This observation can be readily demonstrated by considering
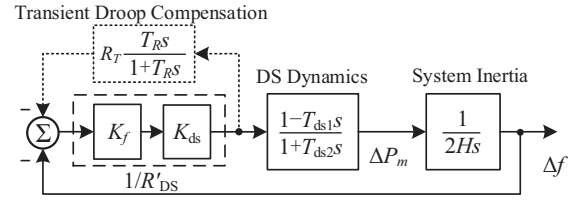

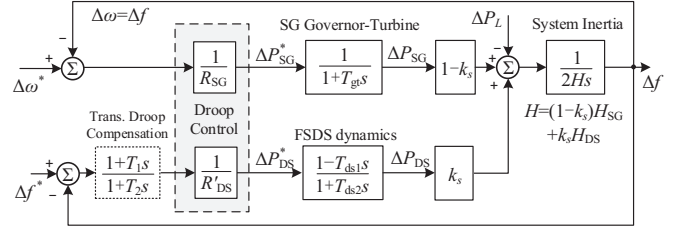Fig. 8. FSDS primary frequency control loop in an isolated power system.

Fig. 9. Block diagram of the frequency regulation system in grid system.

the primary frequency control loop of Fig. 8. It pertains to the situation when the FSDS operates in an isolated system. The FSDS is represented by the transfer function (26) and H is the inertia constant of the power system. The characteristic equation of the closed-loop system is

$$2R'_{DS}HT_{ds2}s^2 + (2R'_{DS}H - T_{ds1})s + 1 = 0 \quad (28)$$

For stable operation, the Routh-Hurwitz criterion requires

$$R'_{DS} > T_{ds1}/(2H) = R'_{DS,cr} \quad (29)$$

As an illustration, the critical droop $R'_{DS,cr}$ is also shown plotted against I in Fig. 7. It can be seen that in this instance, the condition (29) cannot be met when $I > 0.28$ p.u., i.e., to the right of the point X in Fig. 7. The example illustrates the important finding that in general, stability of the power system will be compromised once the insolation level of the FSDS exceeds a particular level. This applies when the adaptive droop is the only mechanism used to effect primary frequency control.

While the isolated system example is useful in illustrating the destabilizing impact of the NMP characteristic of the FSDS, a more complete analysis would be needed for the more realistic situation of grid-connected FSDS. This is shown in the next subsection.

B. FSDS Primary Frequency Control in Grid System

When a FSDS power plant is interconnected into a grid system, the primary frequency control action contributed by the FSDS can be analyzed in a convenient manner by considering an equivalent synchronous generator (SG) operates in parallel with the FSDS power plant. The SG has the permanent droop setting of R_{SG} whereas its governor-turbine system is represented simply by a first-order model

$$M_{gt}(s) = 1/(T_{gt}s + 1) \quad (30)$$

where T_{gt} is the SG governor-turbine time constant. In the grid frequency control block diagram shown on Fig. 9, the
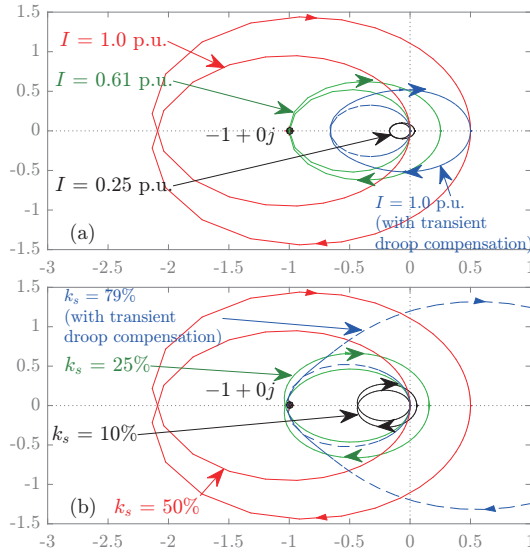
Fig. 10. Nyquist diagrams: (a) $k_s = 50\%$ at various values of I; (b) $I = 1.0$. p.u. at various values of k_s.

frequency deviation Δf is the result of the load change ΔP_L. The combined inertia constant H of the system is calculated based on the total generating capacity $S_{N,\text{tot}} = S_{N,\text{SG}} + S_{N,\text{DS}}$ where $S_{N,\text{SG}}$ and $S_{N,\text{DS}}$ are the generating capacity of the SG and FSDS respectively. The coefficient $k_s = S_{N,\text{DS}}/S_{N,\text{tot}}$ is referred to herewith as the the penetration level of the FSDS solar-thermal generation in the grid system.

From Fig. 9, one can readily carry out a small-signal analysis when the FSDS is under the droop control mode. The open-loop transfer function between the frequency deviation $\Delta f(s)$ and DS plant power, denoted by ΔP_{DS} instead of ΔP_m, can be derived

$$\frac{\Delta f(s)}{\Delta P_{\text{DS}}(s)} = \frac{k_s R_{\text{SG}}}{1 - k_s} \frac{1 + T_{\text{gt}}s}{1 + 2HR_{\text{SG}}s(1 + T_{\text{gt}}s)/(1 - k_s)}. \quad (31)$$

Nyquist analysis is the most effective open-loop method to determine the stability of the power system. One can construct the Nyquist diagram for various insolation and FSDS penetration levels. Again based on the parameters given in the Appendix B, the results are as shown in Fig. 10.

As the number of poles of the open loop system on the RHP is zero in this instance, therefore based on the Nyquist stability criterion, the closed-loop system is stable if and only if the number of clockwise encirclements of the Nyquist contour around the point $-1 + 0j$ is also zero. In this example, Fig. 10 (a) indicates that the system becomes unstable if I is above 0.61 p.u. at penetration level of 50%. On the other hand, Fig. 10 (b) shows that the system would be unstable if k_s is above 25% when I is at the maximum. The example demonstrates that high insolation and/or penetration levels tend to lead to instability. Thus the upper limit $k_{s,\max}$ of FSDS penetration level k_s is 25% in this example, if no other control measures are taken.

To further examine the limit placed on the FSDS penetration level, one can use (26), (27), and (31) to obtain the characteristic equation $\Delta(s)$ of the power system shown in Fig. 9,

viz.,

$$\Delta(s) = a_3 s^3 + a_2 s^2 + a_1 s + a_0 \quad (32)$$

where

$a_3 = 2HR_{\text{SG}}T_{\text{gt}}T_{\text{ds2}}$

$a_2 = 2HR_{\text{SG}}(T_{\text{gt}} + T_{\text{ds2}}) - k_s T_{\text{gt}}T_{\text{ds1}}(R_{\text{SG}}/R'_{\text{DS}})$

$a_1 = 2HR_{\text{SG}} + T_{\text{ds2}} - k_s T_{\text{ds2}} + k_s(R_{\text{SG}}/R'_{\text{DS}})(T_{\text{gt}} - T_{\text{ds1}})$

$a_0 = 1 + k_s(R_{\text{SG}}/R'_{\text{DS}} - 1)$.

The maximum FSDS penetration level $k_{s,\max}$ for guaranteed stable operation can be calculated according to the Routh–Hurwitz analysis. As it can be readily proven that a_3 and a_0 are always greater than zero, one needs to only examine the remaining three necessary and sufficient conditions for stability: $a_1 > 0$, $a_2 > 0$ and $a_2 a_1 - a_3 a_0 > 0$ to derive $k_{s,\max}$. Indeed, it can be shown that $k_{s,\max}$ is about 25% when $R_{\text{DS}} = 0.1$ and when I is maximum. This is in agreement with the outcome of the Nyquist analysis. On the other hand, if a more stringent primary frequency control is required, i.e., R_{DS} reduces, $k_{s,\max}$ will correspondingly decrease. For example, for $R_{\text{DS}} = 0.05$, $k_{s,\max}$ drops to about 10%. Also, the above analysis demonstrates that for a given grid code requirement on the droop setting R_{DS}, the most onerous primary frequency control condition corresponds to that when the FSDS operates under the maximum insolation level.

C. An Enhanced Droop Primary Frequency Control Scheme

Notwithstanding the encouraging outcome using the adaptive droop frequency control scheme, consider next the use of a compensator to provide additional stabilization action in order to counter-act the destabilizing effect of the NMP characteristics of the FSDS. Indeed, similar situation has been encountered in the design of the control system for the hydro-turbine speed regulation system in [17] where transient droop compensation has been applied. The compensator structure is shown in Fig. 8, in which R_T denotes the temporary droop setting and T_R is the reset time. Whence with the droop setting R'_{DS} and the transient droop compensation, the resulting equivalent transfer function of FSDS frequency controller becomes

$$G_c(s) = \frac{1}{R'_{\text{DS}}} \frac{1 + T_R s}{1 + (1 + \frac{R_T}{R'_{\text{DS}}})T_R s} = \frac{1}{R'_{\text{DS}}} \frac{1 + T_1 s}{1 + T_2 s} \quad (33)$$

With the compensation, the droop is increased temporarily from R'_{DS} to $R'_{\text{DS}} + R_T$ at the initial stage of the transient. Using Routh-Hurwitz stability criterion, the range of R'_{DS} for the stable closed-loop system becomes

$$R'_{\text{DS}} > \max\left\{ \frac{T_{\text{ds1}}}{2H} \frac{1}{1 + \frac{R_T}{R'_{\text{DS}}}}, \frac{T_{\text{ds1}} - T_R}{2H + (1 + \frac{R_T}{R'_{\text{DS}}})T_R} \right\} \quad (34)$$

Compare to the condition (29), the droop determined by (38) is smaller. This means the stability margin of the power system has been improved by the compensator. On the setting of T_R and R_T, one has to ensure that the break frequency of the compensator is higher than $1/(2H)$ but lower than the original cut-off frequency ω_c of the uncompensated system,

TABLE I
PARAMETRIC VALUES OF PRIMARY FREQUENCY CONTROL

I	0.22–0.4 p.u.	0.4–0.65 p.u.	0.65–1.0 p.u.
$T_{h,\text{set}}$	1.08	0.89	0.81
$D_p/D_{p,\text{AF}}$	14.7	8.5	3.3
K_f	7	10	12

i.e., $1/\omega_c < T_R < (1 + R_T/R'_{\text{DS}})T_R < 2H$. Note as the input signal of the compensator shown in Fig. 8 is not directly measurable, the compensator is to be implemented using the equivalent lag compensator given in (33) and included in Fig. 9, with $T_1 < T_2$. As an illustration of using this compensator, select $T_R = 1$ s and $R_T = 3R'_{\text{DS}}$. With the compensator in place, Fig. 10(a) shows that for penetration level k_s of up to 50%, the system is inherently stable. Indeed from Fig. 10(b), $k_{s,\text{max}}$ for guaranteed stable operation has been increased to 79%.

VI. NUMERICAL EXAMPLES

The purpose of this section is to illustrate the performance of the FSDS when it participates in primary frequency control of grid systems.

A. FSDS Model Validation

In this subsection, the aim is to validate the accuracy of the developed FSDS model. The nonlinear average-value FSDS model derived in Section II is firstly compared with that based on the multi-cylinder adiabatic model of the Stirling engine given in [11]. This latter model is denoted herewith as the detailed adiabatic FSDS model and is considered to be the most accurate DS dynamic simulation model reported in the literature. The external power system is represented by the simplified grid model described in Section V-B. The schematic diagram of the test grid system is shown in Fig. 11. The parametric values of the relevant parameters of the FSDS and SG are those used in the examples of the previous sections. See Appendix B. It is assumed that the penetration level k_s is 20% which is below the highest penetration level $k_{s,\text{max}}$ permissible for stable operation obtained in Section V-B. The capacities of the SG and DS are $S_{N,\text{SG}} = 800$ MW, and $S_{N,\text{DS}} = 200$ MW respectively. The initial load is assumed to be 820 MW. The insolation level is 1.0 p.u. for which $P_{\text{DS}} = 0.18$ and $P_{\text{SG}} = 0.64$ p.u. on $S_{N,\text{tot}}$ of 1000 MW base. The deloaded curve A′C was approximated by a piecewise linear curve consisting of three segments A′K$_1$, K$_1$K$_2$, and K$_2$C as shown in Fig. 1 and corresponding values of the control parameters D_p, $T_{h,\text{set}}$, and K_f are given in Table I.

At $t = 5$ s, a load increase ΔP_L of 150 MW is applied. Fig. 12 shows the waveforms obtained using the various FSDS models. It can be seen that using the developed average-value nonlinear FSDS model, the most important and pertinent characteristics of the FSDS under the primary frequency control regime have been effectively captured and reproduced. Indeed, Fig. 12 show there is close agreement between the results obtained using the developed average-value FSDS model with that based on the detailed adiabatic
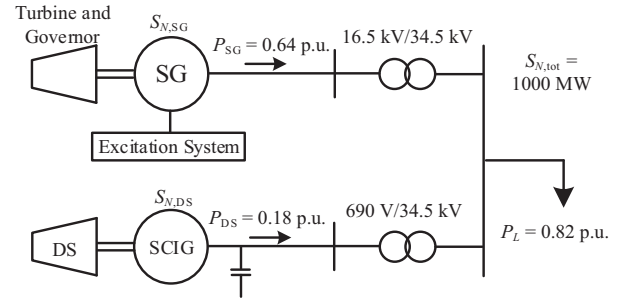

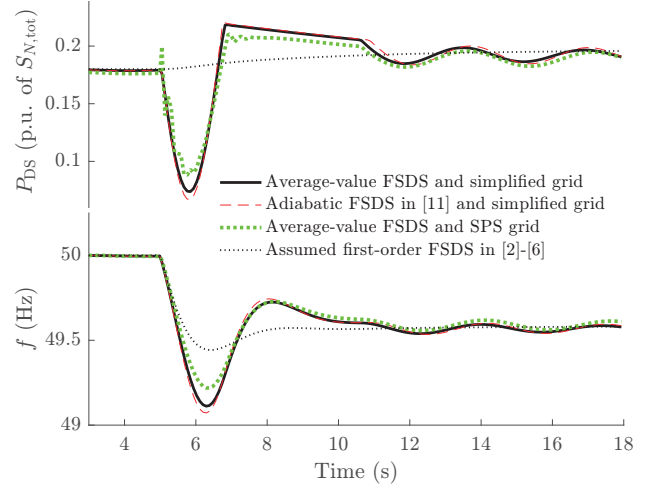Fig. 11.   System configuration for simulation validation.

Fig. 12.   Comparison of simulation results using different FSDS models.

FSDS model. This is an encouraging outcome because the step-size used in generating the time-response of the developed FSDS is compatible with that required for grid frequency control studies which involve the electromechanical transient. This is in contrast to the detailed adiabatic DS model which requires much smaller step-size of the order to 2 μs to simulate the internal thermodynamic behaviors of the Stirling engine. In this example, the small step-size results in very high computational burden and requires some 670 s to complete the simulation whereas in using the developed average-value model, the total computation time is only 5.2 s.

The results obtained using the assumed first-order DS model proposed in [2]–[6] are also included in Fig. 12. It is very clear the first-order DS model used in these references is unsuitable for use in the primary frequency control study as the response of the FSDS is vastly different from that obtained using the detailed adiabatic model. Additionally, a detailed electromagnetic transient model established using Simscape Power Systems (SPS) blockset in MATLAB/Simulink environment is incorporated in the study. The SPS model includes synchronous generator, turbine and governor, generator excitation system, among other power system components. From Fig. 12, it can be seen that essentially, the results based on the simplified grid model are in agreement with those obtained using the SPS model. The initial fast electromagnetic oscillating transient components obtained based on the SPS model are due to the presence of short-duration voltage perturbations. In

frequency control study, voltage variations are not considered as they do not bear much impact on the subsequent frequency perturbations, as is borne out in Fig. 12.

In the view of above, the proposed nonlinear average-value FSDS model and the simplified grid model will be used in the following numerical examples.

B. Primary Frequency Control Following a Step Load Change

In this case study, the same step load change as described in Section VI-A is assumed. The results of the simulation are shown in Figs. 13(a)–(c) for the three scenarios: 1) FSDS does not participate in primary frequency control; 2) FSDS provides primary frequency control ancillary service, effected through the droop control scheme shown in Fig. 9; 3) Same as scenario 2 but with the additional transient droop compensation.

From Fig. 13(b), it can be seen that if no primary frequency control action is provided by the FSDS, the steady-state frequency deviation is 0.47 Hz. When the FSDS participates in the primary frequency control, the FSDS increases its output power from 0.18 p.u. to about 0.192 p.u. and the system frequency deviation is correspondingly reduced to 0.43 Hz.

It can be seen from Fig. 13(a) that when the primary frequency control is brought in, the FSDS decreases its power at the initial stage of the transient (undershoot) which is opposite to the increase in the power level at the steady-state. This is due to the NMP characteristics of FSDS. The initial relatively large decrease in the power counteracts the inertia response from the generator-turbine of the SG. After the initial stage, there is a period of poorly-damped and undesirable oscillations in the power and receiver temperature. With the transient droop compensation and selected control parameters, the power undershoot is greatly reduced and the persistent oscillations have been removed. Indeed, Fig. 13(b) shows that the transient droop compensation has raised appreciably the nadir of the frequency from 49.1 Hz to about 49.4 Hz and the primary frequency response from the FSDS is essentially accomplished in about 10 s.

The above cases are repeated but with the FSDS penetration level k_s increased to 50% which is above $k_{s,\max}$ of 25% predicted in the previous section. The outcome of the simulation is as shown in Figs. 13(d)–(f). It confirms that the power system is unstable if the transient droop compensator is not used. The receiver temperature can rise to high value and can be damaging to the receiver/absorber. With the transient droop compensator, the system is well-damped and the temperature is well controlled. The FSDS is seen to carry out the primary frequency control task satisfactorily.

C. Primary Frequency Control Under Perturbing Insolation

With the same system configuration and control parameters as in Section IV-A, the impact of insolation variations on the performance of the primary frequency control of the FSDS is investigated next. I is assumed to start at 1 p.u. level and reduces to 0.4 p.u. in a 0.2 p.u. step every 20 s. I is then restored back to the 1.0 p.u. level in the reverse manner. The simulation results for $k_s = 20\%$ and 50% are shown in Fig. 14. It can be seen that the proposed adaptive
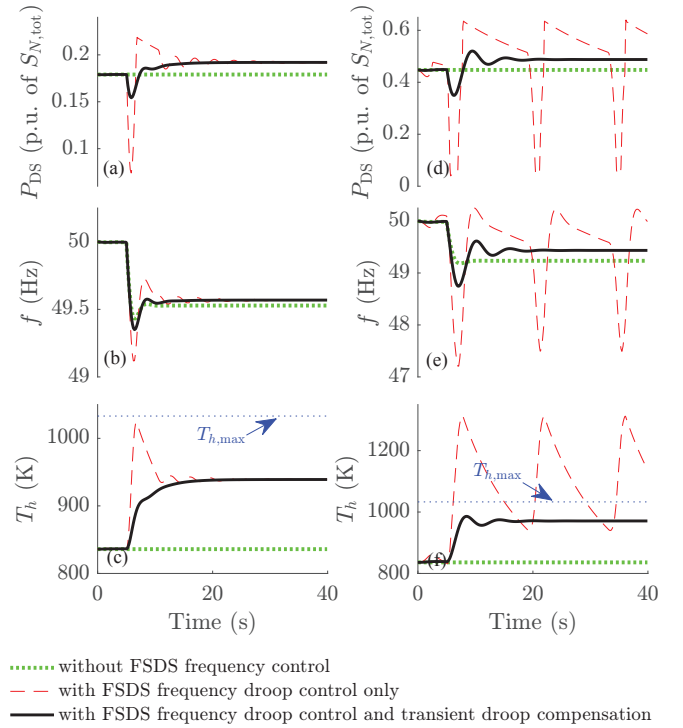

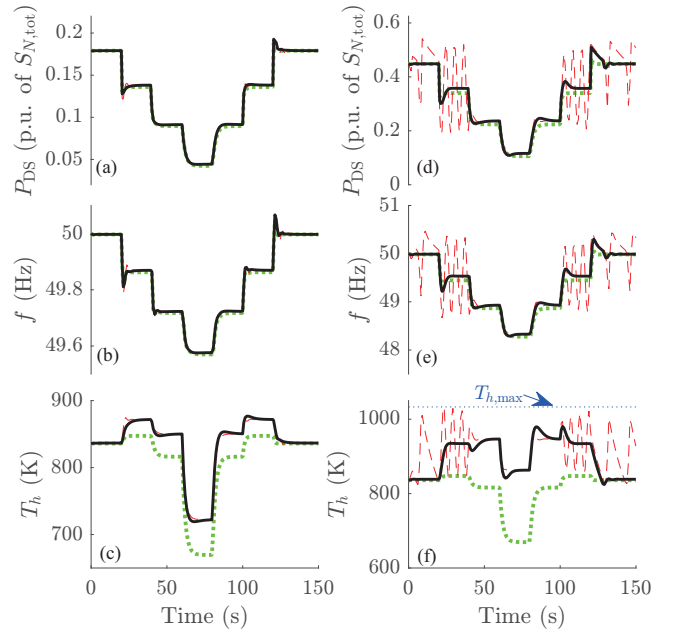Fig. 13. Primary frequency response to step load change for: (a)–(c) $k_s = 20\%$; (d)–(f) $k_s = 50\%$.

..... without FSDS frequency control
– – with FSDS frequency droop control only
—— with FSDS frequency droop control and transient droop compensation

Fig. 14. Primary frequency response as insolation varies for: (a)–(c) $k_s = 20\%$; and (d)–(f) $k_s = 50\%$. Legends for the curves are the same as that in Fig. 13.

supplementary control loop with transient droop compensation control scheme can provide primary frequency support with acceptable steady-state and dynamic performance even under the $k_s = 50\%$ penetration level condition. As has been stated before, the controller designed at the maximum insolation level performs better under lower I levels because the stability
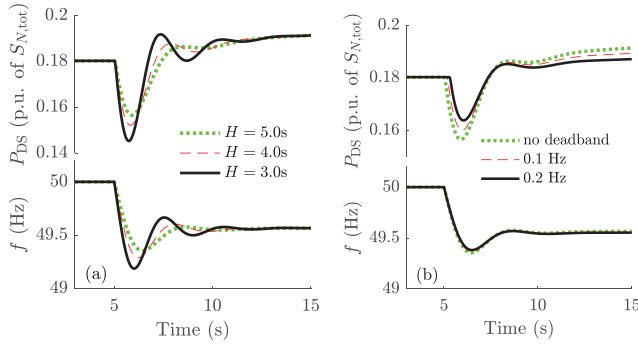
Fig. 15. Test of robustness of the developed FSDS primary frequency control scheme by considering system parameter variations of (a) system inertia H and (b) dead-band setting in the power-frequency droop line.

margin is larger at the lower I levels.

D. Robustness of Proposed Control Scheme

In order to test the robustness of the proposed adaptive droop primary frequency control scheme, the performance of the power system under several uncertain parameter conditions is also investigated. These parameter variations include that of system inertia H, and the dead-band in the power-frequency droop line. The simulation results, given in Fig. 15, show that within the studied parameter variation bands, the developed control scheme has achieved acceptable performance in the course of the primary frequency control. As expected, the larger inertia has resulted in less severe frequency deviations while the presence of the dead band has led to smaller perturbations in the system frequency. The robustness of the frequency controller has also been tested on other system parameter variations, including the permanent droop R_{SG} of the SG unit and turbine-generator constant T_{gt}, and various DS parameters that affects the equivalent coefficient K_{ds}, T_{ds1}, and T_{ds2}. In general, the power system performance is seen to be insignificantly affected by up to 50% of variations of these parameters.

VII. CONCLUSIONS

By allowing the working temperature of the receiver to vary, the ability of fixed-speed dish-Stirling system to provide primary frequency control has been investigated. The conventional frequency-power droop control scheme is supplemented by an adaptive control loop to cater for the need to adjust the set-point of the receiver temperature as the insolation level varies. From the developed model, the FSDS is shown to exhibit the destabilizing nonminimum phase characteristic. As a result, the penetration level of the generator has to be limited to ensure stable operation of the primary frequency control scheme. The droop controller is also to be tuned under the most onerous condition of maximum insolation level. Next, it is established that transient droop compensation can augment the droop control scheme to allow higher penetration level of the solar-thermal generation.

The tuning of the transient droop compensator to accommodate the uncertain input solar power remains a challenging task and should be a fruitful area for further work.

APPENDIX A

The heat losses equation of the concentrator/receiver is [18]

$$Q_L = A_{rec}U(T_h - T_a) + A_{rec}\varepsilon\sigma_B(T_h^4 - T_a^4). \quad (35)$$

The first and the second terms on the RHS of (35) are the power losses due to convection/conduction and radiation respectively. A_{rec} is the area of the receiver aperture, U is the receiver overall heat-loss coefficient, ε is the emittance of receiver, and σ_B is the Stefan-Boltzmann constant. Choosing the maximum temperature $T_{h,max}$ and nominal engine power $P_{m,N}$ as the base values, (35) can be normalized as

$$\bar{Q}_L = K_{rec1}(\bar{T}_h - \bar{T}_a) + K_{rec2}(\bar{T}_h^4 - \bar{T}_a^4) \quad (36)$$

where coefficients K_{rec1} and K_{rec2} are given as

$$K_{rec1} = \frac{T_{h,max}A_{rec}U}{P_{m,N}}, K_{rec2} = \frac{T_{h,max}^4 A_{rec}\varepsilon\sigma_B}{P_{m,N}}.$$

In the main text, the overbar that represents the per-unit quantity will be removed for simplicity of notation.

APPENDIX B

The following parameters were obtained from [7], [8], [17].
Each Single 27-kW Dish/Receiver Unit: $A_{rec} = 0.0314$ m^2, $U = 395.3$ W/(m^2·K), $\sigma_B = 5.67\times10^{-8}$ W/(m^2·K^4), $\varepsilon = 0.9$, $T_{h,max} = 1033$ K, $P_{m,N} = 27$ kW.
Normalized FSDS Parameters: $K_{con} = 1.756$, $T_{rec} = 13.436$ s, $K_{rec} = 2.865$, $K_{rec1} = 0.4751$, $K_{rec2} = 0.0677$, $a_{00} = 0.045$, $a_{10} = 0.068$, $a_{01} = 0.20$, $a_{11} = 2.14$, $b_{00} = -0.038$, $b_{10} = -0.072$, $b_{01} = 0.055$, $b_{11} = 1.21$, $b_{02} = -0.026$, $b_{12} = -0.13$, $A = -0.2735$, $C = 0.8752$, $K_h = 2.8274$, $K_m = 1.8505$, $k_{m0} = -0.715$, $k_{m1} = 2.906$, $k_{m2} = -1.191$, $d_{00} = 0.0064$, $d_{01} = -0.0261$, $d_{02} = 0.0107$, $d_{10} = -0.7214$, $d_{11} = 2.9321$, $d_{12} = -1.2017$, $T_{h,low} = 0.5$ p.u., $T_k = 0.313$ p.u., $p_{max} = 1$ p.u., $p'_{max} = 1.1$ p.u., $p_{min} = 0.1$ p.u., $K_v = 1$, $T_v = 0.02$ s, $K_p = 1.0$ p.u., $D_{p,AF} = 0.043$, $K_{MPC} = 25$, $T_1 = 1$ s, $T_2 = 4$ s, $x\% = 10\%$, $R_{DS} = 0.1$.
Equivalent SG Unit: $H = 5.0$ s, $R_{SG} = 0.05$, $T_{gt} = 0.5$ s, $f_1 = 49.5/50$ p.u. For the description of SPS for detailed SG/grid model, readers may refer to [17], [19].

APPENDIX C

Consider $\omega_m = 1$ p.u., by linearizing the model (1), (3)–(7), (9), (10), (17), (18), and (24) at a specific steady-state operating point of $I = I_0$, $T_h = T_{h0}$, and $p_{mean} = p_0$, one can obtain the following small-signal FSDS model.

$$\Delta Q_h = (a_{10} + a_{11})\Delta p_{mean} + \eta_{h0}A\Delta gA + \eta_{h0}Cp_0\Delta\dot{T}_h \quad (37)$$

$$(T_{rec}/K_{rec})\Delta\dot{T}_h + (K_{rec1} + 4K_{rec2}T_{h0}^3)\Delta T_h = -\Delta Q_h \quad (38)$$

$$\Delta P_m = (d_{01} + 2d_{02}T_{h0} + d_{11}p_0 + 2d_{12}T_{h0}p_0)\Delta T_h$$
$$+ (d_{10} + d_{11}T_{h0} + d_{12}T_{h0}^2)\Delta p_{mean} \quad (39)$$

$$\Delta p_{mean} \approx \Delta p_{mean}^* = -(\Delta T_{h,set} + \Delta T_h)/D_p \quad (40)$$

$$\frac{\Delta gA}{\Delta p_{mean}^*} = \frac{1}{K_p}\frac{s}{2T_vs(1 + T_vs) + 1} \approx \frac{s}{2T_vs + 1} \quad (41)$$

where η_{h0} is the value of η_h at this steady-state point. Using (37), (38), (40), and (41) to eliminate Q_h, gA, and p_{mean}, the transfer function between T_h and $T_{h,\text{set}}$ is obtained, i.e.,

$$\frac{\Delta T_h(s)}{\Delta T_{h,\text{set}}(s)} = \frac{v(2T_v s + 1) + \eta_{h0} A s}{ws(2T_v s + 1) + z(2T_v s + 1) + \eta_{h0} A s} \quad (42)$$

where

$$v = a_{10} + a_{11}, \quad z = D_p(K_{\text{rec1}} + 4K_{\text{rec2}}T_{h0}^3) + v,$$

$$w = D_p(T_{\text{rec}}/K_{\text{rec}} + \eta_{h0} C p_{\text{set}})$$

Next, substituting (42) and (40) into (39), the transfer function between P_m and $T_{h,\text{set}}$ is derived. Ignoring the second-order terms, thus

$$\Delta P_m(s)/\Delta T_{h,\text{set}}(s) = K_{\text{ds}}(1 - T_{\text{ds}1}s)/(1 + T_{\text{ds}2}s) \quad (43)$$

where

$$T_{\text{ds}1} = \frac{2T_v xv + x\eta_{h0}A - 2T_v zy - \eta_{h0}Ay - wy}{zy - xv} \approx \frac{-wy}{zy - xv},$$

$$T_{\text{ds}2} = D_p(T_{\text{rec}}/K_{\text{rec}})/(a_{10} + a_{11}) + 2T_v,$$

$$K_{\text{ds}} = -y + xv/z, \quad y = (d_{10} + d_{11}T_{h0} + d_{12}T_{h0}^2)/D_p,$$

$$x = d_{01} + 2d_{02}T_{h0} + d_{11}p_0 + 2d_{12}T_{h0}p_0 + y.$$

REFERENCES

[1] T. Mancini, P. Heller, B. Butler, B. Osborn, W. Schiel, V. Goldberg, R. Buck, R. Diver, C. Andraka, and J. Moreno, "Dish-Stirling systems: An overview of development and status," *ASME J. Solar Energy Eng.*, vol. 125, no. 2, pp. 135–151, May 2003.

[2] D. C. Das, N. Sinha, and A. K. Roy, "Small signal stability analysis of dish-Stirling solar thermal based autonomous hybrid energy system," *Int. J. Elec. Power Energy Syst.*, vol. 63, pp. 485–498, Dec. 2014.

[3] A. Rahman, L. C. Saikia, and N. Sinha, "AGC of dish-Stirling solar thermal integrated thermal system with biogeography based optimised three degree of freedom PID controller," *IET Renew. Power Gen.*, vol. 10, no. 8, pp. 1161–1170, Sep. 2016.

[4] A. Rahman, L. C. Saikia, and N. Sinha, "Automatic generation control of an interconnected two-area hybrid thermal system considering dish-Stirling solar thermal and wind turbine system," *Renew. Energy*, vol. 105, pp. 41–54, May 2017.

[5] I. Hussain, D. C. Das, and N. Sinha, "Reactive power performance analysis of dish-Stirling solar thermal-diesel hybrid energy system," *IET Renew. Power Gen.*, vol. 11, no. 6, pp. 750–762, May 2017.

[6] D. Santos-Martin, J. Alonso-Martinez, J. Eloy-Garcia, and S. Arnalte, "Solar dish-Stirling system optimisation with a doubly fed induction generator," *IET Renew. Power Gen.*, vol. 6, no. 4, pp. 276–288, Jul. 2012.

[7] Y. Li, S. S. Choi, C. Yang, and F. Wei, "Design of variable-speed dish-Stirling solar-thermal power plant for maximum energy harness," *IEEE Trans. Energy Convers.*, vol. 30, no. 1, pp. 394–403, Mar. 2015.

[8] Y. Li, S. S. Choi, and C. Yang, "Dish-Stirling solar power plants: Modeling, analysis and control of receiver temperature," *IEEE Trans. Sustain. Energy*, vol. 5, no. 2, pp. 398–407, Apr. 2014.

[9] Y. Li, S. S. Choi, and C. Yang, "An average-value model of kinematic Stirling engine for the study of variable-speed operations of dish-Stirling solar-thermal generating system," in *Proc. IEEE Int. Conf. Control Autom.*, Taichung, Taiwan, Jun. 2014, pp. 1310–1315.

[10] D. G. Thombare and S. K. Verma, "Technological development in the Stirling cycle engines," *Renew. Sustain. Energy Rev.*, vol. 12, no. 1, pp. 1–38, Jan. 2008.

[11] D. Howard and R. G. Harley, "Modeling of dish-Stirling solar thermal power generation," in *Proc. IEEE Power and Energy Soc. General Meeting*, Minneapolis, MN, USA, Jul. 2010, pp. 1–7.

[12] D. F. Howard, J. Liang, and R. G. Harley, "Control of receiver temperature and shaft speed in dish-Stirling solar power plants to meet grid integration requirements," in *Proc. IEEE Energy Convers. Congr. Expo.*, Atlanta, GA, USA, Sep. 2010, pp. 398–405.

[13] B. Kongtragool and S. Wongwises, "A review of solar-powered Stirling engines and low temperature differential Stirling engines," *Renew. Sustain. Energy Rev.*, vol. 7, no. 2, pp. 131–154, Apr. 2003.

[14] W. B. Stine and R. W. Harrigan, *Solar Energy Fundamentals and Designs - with Computer Applications.* Sommerset, NJ, USA: John Wiley & Sons, 1985.

[15] ENTSO-E, "ENTSO-E network code on requirements for grid connection applicable to all generators," 2013.

[16] "Technical regulation 3.2.5 for wind power plants with a power output greater than 11 kW," Jun. 2016.

[17] P. Kundur, N. J. Balu, and M. G. Lauby, *Power System Stability and Control.* New York, NY, USA: McGraw-Hill, 1994.

[18] W. B. Stine and R. B. Diver, "A compendium of solar dish/Stirling technology," Sandia National Laboratories, Tech. Rep. SAND93-7026 UC-236, Jan. 1994.

[19] MathWorks, "Simscape power systems reference (specialized technology)," pp. 5–270,5–239,5–79,5–86,5–340,5–313,5–26, Mar. 2017.

Yang Li (S'11–M'16) received the B.E. degree in electrical engineering from Wuhan University, Wuhan, China, in 2007 and the M.Sc. and Ph.D. degrees in power engineering from Nanyang Technological University (NTU), Singapore, in 2008 and 2015, respectively.

From 2015 to 2016, he was with the Energy Research Institute, NTU. He is now a Research Fellow with the School of Electrical Engineering and Computer Science, Queensland University of Technology, Brisbane, Australia.

His research interests include renewable energy systems, power system control, energy storage systems, and power electronic converters.

San Shing Choi (M'03–SM'07) received the B.E. and Ph.D. degrees in electrical engineering from the University of Canterbury, Christchurch, New Zealand, in 1973 and 1976, respectively.

He was previously with the New Zealand Electricity Department, Wellington, New Zealand, National University of Singapore, Singapore and the State Energy Commission of Western Australia, Perth, Australia, and the Nanyang Technological University, Singapore. He is now an Adjunct Professor at the University of Western Australia, as well as that of Curtin University of Technology and Queensland University of Technology, Australia.

His research interests include power system control, renewable and energy storage systems.

D. Mahinda Vilathgamuwa (S'90–M'93–SM'99) received the B.Sc. degree in electrical engineering from the University of Moratuwa, Moratuwa, Sri Lanka, in 1985 and the Ph.D. degree in electrical engineering from Cambridge University, Cambridge, U.K., in 1993. In 1993, he joined the School of Electrical and Electronic Engineering, Nanyang Technological University, Singapore, as a Lecturer and then became an Associate Professor. He is currently a Professor with the Queensland University of Technology, Brisbane, Australia.

His current research interests include power electronic converters, electrical drives, and power quality.